Journal of
Materials Chemistry A

ROYAL SOCIETY
OF CHEMISTRY

PAPER

View Article Online
View Journal | View Issue

Check for updates

Cite this: *J. Mater. Chem. A*, 2026, **14**, 16218

Open Access Article. Published on 13 March 2026. Downloaded on 6/14/2026 12:25:04 PM.
This article is licensed under a Creative Commons Attribution-NonCommercial 3.0 Unported Licence.

Elucidating the structure–performance relationship in single-particle NCM cathodes *via* controlled precursor synthesis

Soonhyun Hong,†[a] Heesang Lee, †[a] Jahun Koo,[a] Wonchan Hwang,[b]
Ji Hwan Kim,[bcd] Yung-Eun Sung, [cd] Jungjin Park, *[b] Young-Sang Yu*[ef]
and Chunjoong Kim*[a]

Received 15th December 2025
Accepted 10th March 2026

DOI: 10.1039/d5ta10228f

rsc.li/materials-a

While high-energy-density Ni-rich layered oxides, $LiNi_{1-x-y}Co_xMn_yO_2$ (Ni > 0.8), are of significant attention as next-generation cathode materials, their practical application is limited by intergranular cracking and mechanical degradation arising from anisotropic lattice strain. The single-particle cathode strategy has emerged as a promising solution, effectively suppressing intergranular cracking by eliminating boundaries between primary particles. However, the fundamental relationships between single-particle size, internal microstructure, and electrochemical performance remain poorly understood. Here, we present a molten-salt synthesis strategy to produce $LiNi_{0.92}Co_{0.03}Mn_{0.05}O_2$ single-particle cathodes with tunable particle and crystallite sizes *via* precursor morphology control. Systematic analysis reveals clear correlations between precursor shape, final particle microstructure, and rate capability. This work aims to establish the causal link between precursor morphology, final particle microstructure, and electrochemical performance, thereby providing a core design principle for developing high-stability and -power single-particle cathode materials.

1. Introduction

Recently, the blueprint for net-zero carbon emissions has been announced as part of a global effort against climate change.[1] Based on the comprehensive carbon emission reduction plan, electric vehicles (EVs) are projected to occupy approximately 77% of the global automobile market by 2030.[2] Accordingly, the demand for high-performance lithium-ion batteries (LIBs) that can power EVs is rapidly increasing. The most promising candidate is still the layered oxide with a high nickel concentration (Ni content >80 at% in the composition of the transition metals), Ni-rich $LiNi_{1-x-y}Co_xMn_yO_2$ (Ni-rich NCM), which is derived from the first commercialized cathode material, $LiCoO_2$.[3,4] Despite its high theoretical capacity (>200 mA h g^{-1}), the Ni-rich NCM cathode material exhibits intrinsic limitations, including fast capacity fade and safety concerns.[5,6] The origin of capacity fading in commonly used Ni-rich NCM aggregates is the significant volume change of primary particles, which gradually leads to intergranular cracking during repeated cycling.[7,8] The formation and propagation of cracks deteriorate mechanical integrity, ultimately resulting in the loss of electrical contacts.[9] In addition, the cracks keep exposing a fresh surface or interface to the electrolyte, followed by the formation of electrochemically inactive phases.[10,11] Therefore, the emergence of such inactive phases leads to continuous capacity decay as well as sluggish Li^+ transport.[12,13] Therefore, the emergence of such inactive phases leads to continuous capacity decay as well as sluggish Li^+ transport. Such surface accompanied by oxygen loss driven cation migration, forming surface-densified Ni-rich phases that increase interfacial resistance and accelerate performance decay.[14]

Among various strategies such as transition metal (TM) gradient,[15] doping,[16] and surface coating,[17] Ni-rich single-particle NCM (hereafter, SP-NCM) materials stand out as a promising solution. The SP-NCM reveals great potential to enhance mechanical integrity and cycle performance by minimizing particle cracking, gas evolution, and electrolyte reactivity, despite certain handling issues during the manufacturing process.[18–20] Furthermore, the Ni-rich SP-NCM cathode materials are readily applicable to all-solid-state batteries due to their

---

[a] *Department of Materials Science and Engineering, Chungnam National University, 99 Daehak-ro, Yuseong-gu, Daejeon 34134, Republic of Korea. E-mail: ckim0218@cnu.ac.kr*

[b] *Energy Storage Research Center, Clean Energy Research Division, Korea Institute of Science and Technology (KIST), 5 Hwarang-ro, Seongbuk-gu, Seoul 02792, Republic of Korea. E-mail: jpark716@kist.re.kr*

[c] *School of Chemical and Biological Engineering, Seoul National University, Seoul 08826, Republic of Korea*

[d] *Center for Nanoparticle Research, Institute for Basic Science (IBS), Seoul 08826, Republic of Korea*

[e] *Department of Physics, Chungbuk National University, 1 Chungdae-ro, Seowon-gu, Cheongju 28644, Republic of Korea. E-mail: youngsang@chungbuk.ac.kr*

[f] *Advanced Energy Research Institute, Chungbuk National University, 1 Chungdae-ro, Seowon-gu, Cheongju 28644, Republic of Korea*

† S. H. and H. L. contributed equally to this work.

This journal is © The Royal Society of Chemistry 2026

Open Access Article. Published on 13 March 2026. Downloaded on 6/14/2026 12:25:04 PM.
This article is licensed under a Creative Commons Attribution-NonCommercial 3.0 Unported Licence.

curtailed interfacial contact with the electrolyte.[21] However, deliberate control over particle size and morphology in SP-NCM systems remains challenging, since most synthetic routes rely on complex multi-step processes and high-temperature calcination steps.[22–24]

Herein, we firstly propose a rational synthesis protocol that combines coprecipitation of transition-metal precursors with a subsequent molten-salt reaction to synthesize SP-NCM with tunable particle and domain sizes. During the coprecipitation reaction, transition-metal hydroxide, $TM(OH)_2$ (TM = Ni, Co, Mn), was prepared, with the thickness of primary particles manipulated through fine control of the reaction variables.[25–27] The following molten-salt synthesis renders the calcination and sintering of SP-NCM with various particles and domain sizes from the TM hydroxide precursor.[28] Systematic analyses confirmed a strong correlation between the precursor morphology and the resulting single-particle size, as well as a clear dependence of electrochemical performance on both particle and domain sizes. We believe that our work, therefore, provides a fundamental understanding of the structure–performance relationship in SP-NCMs and establishes a generalizable synthesis framework for designing high-performance single-particle cathode materials.

2. Experimental section

2.1. Synthesis of Ni-rich precursor

$Ni_{0.92}Co_{0.03}Mn_{0.05}(OH)_2$ precursors were synthesized using the coprecipitation method. A 1.5 M aqueous solution with a molar ratio of Ni : Co : Mn = 0.92 : 0.03 : 0.05 was prepared using $NiSO_4 \cdot 6H_2O$, $CoSO_4 \cdot 7H_2O$, and $MnSO_4 \cdot H_2O$, respectively. The mixed solution was pumped into a 5 L continuous stirred-tank reactor at a rate of 0.12 mol h^{-1} under a nitrogen atmosphere. Concurrently, aqueous solutions of 4.0 M NaOH and 14.8 M $NH_3 \cdot H_2O$ were introduced to regulate pH (*i.e.*, molar concentration of hydroxyl anions) and concentration of chelating agent, respectively. The pH values of the solution were controlled from 11.2 to 12.1 by adjusting the NaOH feed rate, while the ammonia concentration in the reactor was varied from 0.5 M to 5.0 M. The reaction temperature was maintained at ∼48 °C using a hot water circulation system, and the stirrer was operated at 800 rpm. The reaction was allowed to proceed for 20 hours, yielding spherical $Ni_{0.92}Co_{0.03}Mn_{0.05}(OH)_2$ precursor. The resulting precipitates were filtered using a vacuum filter system and washed with a slightly lower pH NaOH solution and distilled water to remove residual sodium ions. The filtered precipitate was then dried at 80 °C in the convection oven overnight.

2.2. Synthesis of Ni-rich NCM

For the synthesis of single-particle $LiNi_{0.92}Co_{0.03}Mn_{0.05}O_2$ (SP-NCM), three representative $Ni_{0.92}Co_{0.03}Mn_{0.05}(OH)_2$ precursors with distinct morphologies were selected. The corresponding coprecipitation conditions were as follows: 1.0 M NH_3 at a pH of 11.2, 2.0 M NH_3 at a pH of 12.1, and 5.0 M NH_3 at a pH of 12.1. For the following molten-salt reaction, the precursor, $LiOH \cdot H_2O$, and $Li_2SO_4 \cdot H_2O$ were thoroughly mixed with a molar ratio of 1 : 2 : 0.25, respectively. The homogenous mixture was then held at 850 °C for 10 hours under an oxygen atmosphere and slowly cooled to 250 °C. The ramping and cooling rates were set to be 10 °C min^{-1} and 2 °C min^{-1}, respectively. Then, the material was allowed to cool naturally from 250 °C to room temperature (RT). The resulting composite was grounded, washed with distilled water, and centrifuged several times (for 5 min at 5000 rpm each time) to remove residual Li salts. The washed material was dried at 80 °C overnight, heated at 700 °C for 6 hours in oxygen to remove residual water, and then ground once again. The final products are designated as SP-1.0/11.2, SP-2.0/12.1, and SP-5.0/12.1, corresponding to precursor synthesis conditions of 1.0 M NH_3 at a pH 11.2, 2.0 M NH_3 at a pH 12.1, and 5.0 M NH_3 at a pH 12.1 respectively.

2.3. Structural characterizations

The crystallographic structures of the samples were analyzed using X-ray diffractometer (XRD, D8 ADVANCE, Bruker), operated at 40 kV and 40 mA with Cu Kα radiation ($\lambda_{avg} = 1.5406$ Å). The XRD peaks were measured over a range of 10° to 70° at a scan rate of 2° min^{-1} and a scan step of 0.02°. The surface morphology of the prepared samples was examined using scanning electron microscopy (SEM, CLARA, TESCAN) operated at an acceleration voltage of 10 kV. To evaluate the primary particle thickness of the precursors, more than eighty individual primary particles within each aggregated precursor were measured. Likewise, the particle sizes of the SP-NCM samples were estimated from major and minor axes of over fifty individual particles, obtained from SEM images and analyzed using ImageJ software.[29]

2.4. Measurement of the electrochemical performances

The 80 μm-thick working electrode was prepared on 20 μm-thick aluminum foil by casting a slurry, which consists of 80% active material, 10% binder (polyvinylidene fluoride, PVDF), and 10% carbon black (DENKA BLACK) in NMP (*N*-methyl-2-pyrrolidone) solvent. The electrode was dried under a vacuum at 120 °C overnight to evaporate the solvent and then calendared to 50% of the active material thickness. The cathode mass loading was controlled to approximately 3 mg cm^{-2} for most electrodes. Circular electrodes with a 14 mm diameter were punched and accurately weighed. CR2032 coin-type half-cells were assembled using the prepared working electrode as the cathode and a Li metal foil as the anode. Coin cells were assembled using 100 μl of electrolyte and a 25 μm-thick PE monolayer microporous separator. The electrolyte consisted of 1 M $LiPF_6$ dissolved in a mixture of ethylene carbonate (EC), dimethyl carbonate (DMC), and ethyl–methyl carbonate (EMC) (volume ratio 1 : 1 : 1, Donghwa electrolyte). All cell assembly was performed in a high-purity argon-filled glovebox with O_2 and moisture levels below 0.1 ppm. Electrochemical tests were conducted using a WonATech WBCS 3000L system. Galvanostatic charge–discharge cycling was performed with a potential range of 2.7–4.3 V (*vs.* Li^+/Li). The first two cycles were carried

Open Access Article. Published on 13 March 2026. Downloaded on 6/14/2026 12:25:04 PM.
This article is licensed under a Creative Commons Attribution-NonCommercial 3.0 Unported Licence.

out at 0.1C (assuming 1C = 200 mA g^{-1}) at room temperature, and followed by cycling at 1C for additional electrochemical tests. For the long-term cycling stability test at 1C, discharge was conducted at 1C, whereas charge was carried out using a constant–current/constant–voltage (CC/CV) protocol (CC at 1C to 4.3 V followed by a CV hold at 4.3 V until the current decreased to 0.05C). For the rate capability test, both charge and discharge were performed under the CC mode at each current density within 2.7–4.3 V. Rate capability was evaluated by varying current from 20 mA g^{-1} to 2000 mA g^{-1} within the same potential window, recording five electrochemical measurements at each current rate. To further examine Li$^+$ diffusion kinetics, the galvanostatic intermittent titration technique (GITT) was performed over 2.7–4.3 V during five cycles.

3. Results and discussion

The morphological evolution of $Ni_{0.92}Co_{0.03}Mn_{0.05}(OH)_2$ was systematically explored by adjusting concentrations of OH$^-$ and chelating agent (CA), NH_3 (see the Experimental section for methodological details). Since the concentrations of the hydroxyl anion and the CA are main factors governing the formation of atomically homogeneous precursors,[30] both pH and NH_3 concentrations during the coprecipitation reaction were carefully manipulated to ensure desirable morphologies with homogeneous composition of Ni, Co, and Mn ions in $Ni_{0.92}Co_{0.03}Mn_{0.05}(OH)_2$ without formation of individual metal hydroxide phases such as $Ni(OH)_2$, $Co(OH)_2$, and $Mn(OH)_2$.[31] The addition of ammonia retards the precipitation reaction between TM cations and hydroxyl anions. As a result, TM ions undergo two competitive reactions: (1) coprecipitation with hydroxyl anions to form $TM(OH)_2$, and (2) complexation with NH_3 to yield soluble $TM(NH_3)_n{}^{2+}$ species (where n ranges from 4 to 8). The delicate balance between these two reactions determines the nucleation and growth dynamics of the precursors, ultimately governing their morphology and compositional uniformity.

Firstly, the NH_3 concentration was systematically varied (0.5 M, 1.0 M, 1.5 M, 2.0 M, 2.5 M, and 5.0 M) during the coprecipitation reaction while maintaining a constant pH of 12.1. In addition to participating in the complexation reaction with TM cations, NH_3 strongly coordinates to TM cations, particularly on the (001) planes of $TM(OH)_2$.[32] Consequently, increasing the NH_3 concentration impedes vertical crystal growth along the *c*-axis, favoring lateral expansion within the *ab* plane. Therefore, plate-like primary particles predominantly form, as shown in Fig. 1a. With increasing CA concentration from 0.5 M to 2.0 M, the primary particles become progressively thinner, indicating the enhanced formation of plate-like morphology. However, at concentrations above 2.0 M, the $TM(OH)_2$ plates tend to be agglomerated to minimize the surface energy due to the thermodynamic instability of excessively thin plate-like primary particles.[33]

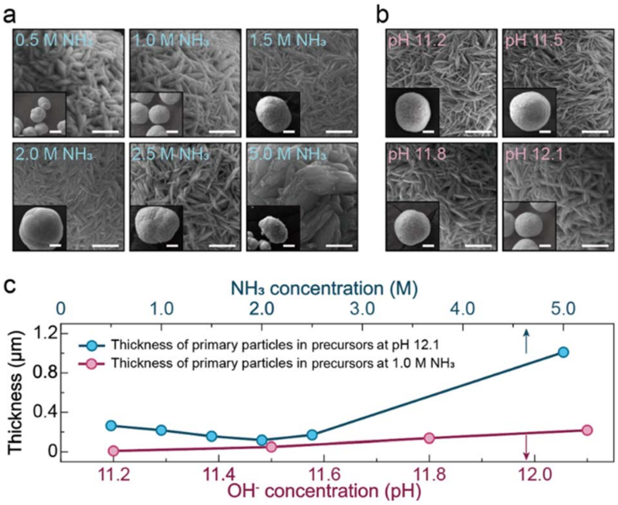

Fig. 1 SEM images of Ni-rich precursors, $Ni_{0.92}Co_{0.03}Mn_{0.05}(OH)_2$, synthesized under various (a) NH_3 concentrations (0.5 M, 1.0 M, 1.5 M, 2.0 M, 2.5 M, and 5.0 M) with a constant pH of 12.1 and (b) OH$^-$ concentrations (pH 11.2, 11.5, 11.8, and 12.1) with a constant NH_3 concentration of 1 M. The scale bar and inset scale bar indicate 1 and 5 μm, respectively. (c) Average thickness of primary particle synthesized under various OH$^-$ (red) and NH_3 (blue) conditions.

Next, the effect of OH$^-$ concentration on precursor morphology was investigated by varying pH values (11.2, 11.5, 11.8, and 12.1) during the coprecipitation reaction under the constant ammonia concentration (1.0 M). As the pH increased from 11.2 to 12.1, the primary particles became thicker along the *c*-axis, which can be attributed to the enhanced reactivity of hydroxyl ions. Under higher OH$^-$ concentration, the coprecipitation of $TM(OH)_2$ is favored over the complexation reaction between TM cations and NH_3, leading to the suppression of (001)-plane coordination by NH_3 on the $TM(OH)_2$ surface (Fig. 1b). A summary of the primary particle thickness as a function of NH_3 and OH$^-$ concentrations is presented in Table 1 and Fig. 1c. The results clearly indicate that both hydroxyl anion and NH_3 concentrations significantly influence the precursor morphology. Thicknesses of primary particles were varied by nearly two orders of magnitude, ranging from approximately 10.4 nm to 1.0 μm, depending on the pH and CA concentrations. The thinnest and thickest primary particles could be obtained from the precursors synthesized at 1.0 M NH_3 at a pH 11.2 and 5.0 M NH_3 at a pH 12.1, respectively. It should be noted that thicker primary particles exhibited stronger aggregation tendency due to their lower anisotropy in the three-dimensional space, resulting in a noticeable difference in the

Table 1 Average thickness of primary particle synthesized under various OH$^-$ and NH_3 conditions

pH[a]	11.2	11.5	11.8	12.1
Ave. thick. [nm]	10.4	50.5	138.2	217.7

NH_3 conc.[b] [M]	0.5	1.0	1.5	2.0	2.5	5.0
Ave. thick. [nm]	264.0	217.7	156.4	117.8	170.4	1010.4

[a] With a constant NH_3 concentration of 1 M. [b] With a constant pH of 12.1.

This journal is © The Royal Society of Chemistry 2026

Open Access Article. Published on 13 March 2026. Downloaded on 6/14/2026 12:25:04 PM.
This article is licensed under a Creative Commons Attribution-NonCommercial 3.0 Unported Licence.

bulk density of the aggregated precursors, as summarized in Fig. S1.

Fig. 2a and b present the powder X-ray diffraction (XRD) patterns of the Ni-rich $Ni_{0.92}Co_{0.03}Mn_{0.05}(OH)_2$ precursors prepared with various CA and hydroxyl concentrations, respectively. All samples exhibit an identical crystal structure, the layered double hydroxide structure with β-$Ni(OH)_2$, which belongs to the space group $P3m1$.[34] The prominent peaks at 2θ of ∼19.15°, ∼33.07°, ∼38.44°, and ∼51.96° are indexed to the (001), (100), (101), and (102) planes, respectively.[35] The relative crystal growth between the $(hk0)$ basal plane and $(00l)$ edge plane can be gauged by the intensity ratios of $R_{(100)/(001)}$, where $R_{x/y}$ represents the ratio between the peak intensities of the x and y planes. Since the (100) diffraction is intrinsically weak due to the low atomic density of transition metals in that plane, $R_{(101)/(001)}$ and $R_{(102)/(001)}$ are also calculated to provide more confident indicators to elucidate the preferential growth of hydroxides.[36] As depicted in Fig. 2c, increasing the pH led to a systematic decrease in $R_{(100)/(001)}$, $R_{(101)/(001)}$, and $R_{(102)/(001)}$, indicating more preferential growth (or stacking) along c-axis over the planar growth along the ab plane. Meanwhile, planar growth along the ab plane is most dominant from the precursors synthesized at the 2.0 M NH_3 concentration, as evidenced by the highest $R_{(100)/(001)}$, $R_{(101)/(001)}$, and $R_{(102)/(001)}$. The inverse trend in diffraction intensity ratios with increasing pH is highly consistent with the microscopic observations of the primary particles (Fig. 1a). A detailed growth mechanism of the $Ni_{0.92}Co_{0.03}Mn_{0.05}(OH)_2$ precursors is beyond the scope of this work and will be addressed in detail in a future study.

Among the $Ni_{0.92}Co_{0.03}Mn_{0.05}(OH)_2$ precursors, three representative precursors exhibiting distinct primary-particle morphology but comparable aggregate sizes (precursors prepared under 1.0 M NH_3 with a pH of 11.2, 2.0 M NH_3 with a pH of 12.1, and 5.0 M NH_3 with a pH of 12.1) were selected to be calcined with $LiOH \cdot H_2O$ to produce single-particle $LiNi_{0.92}Co_{0.03}Mn_{0.05}O_2$ (SP-NCM) as described in the Experimental section. As shown in Table S1, ICP-(AES) confirms that all representative Ni-rich precursors maintain the intended transition-metal stoichiometry (target composition: Ni 0.92, Co 0.03, Mn 0.05). The measured TM fractions show only minor deviations from the target, indicating that varying the synthesis conditions does not induce composition drift and that incomplete complexation is unlikely. N_2 adsorption (BET) measurements were conducted for the same precursors, and the specific surface area and total pore volume are summarized in Table S2. These data are provided to support the discussion on surface-related electrochemical behavior.

As depicted in Fig. 3, the average particle sizes of the resulting SP-NCMs were 1.169 (mean) ± 0.394 (standard deviation) μm, 1.668 ± 0.515 μm, and 4.485 ± 1.052 μm, corresponding to SP-1.0/11.2, SP-2.0/12.1, and SP-5.0/12.1, respectively. The precursor, with its more porous structure composed of thinner primary particles, led to the formation of the smaller SP-NCM particles after the molten-salt reaction, owing to its lower bulk density and higher reactivity during calcination.

In general, the exposed crystal facets of SP-NCMs are highly influenced by the oxygen solubility during the calcination procedure.[37,38] Although all samples were subjected to identical environments during the molten-salt reaction, well-defined truncated octahedron crystal facets were revealed only on the surface of SP-2.0/12.1. In contrast, SP-1.0/11.2 and SP-5.0/12.1 exhibited relatively smooth, featureless surface without

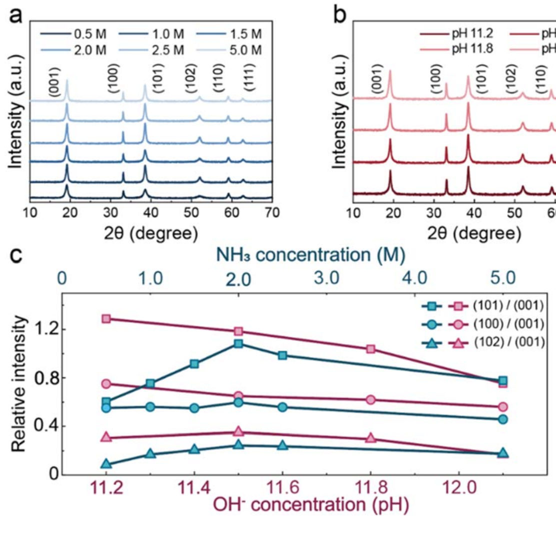

Fig. 2 Structural characterizations of the Ni-rich precursors, $Ni_{0.92}Co_{0.03}Mn_{0.05}(OH)_2$. XRD patterns obtained under varying (a) NH_3 and (b) OH^- concentrations, with the counterpart variables held constant at (a) pH 12.1 and (b) 1.0 M NH_3, respectively. (c) Intensity ratios of (101), (100), and (102) reflections relative to the (001) peak as a function of NH_3 (blue) and OH^- (red) concentrations.

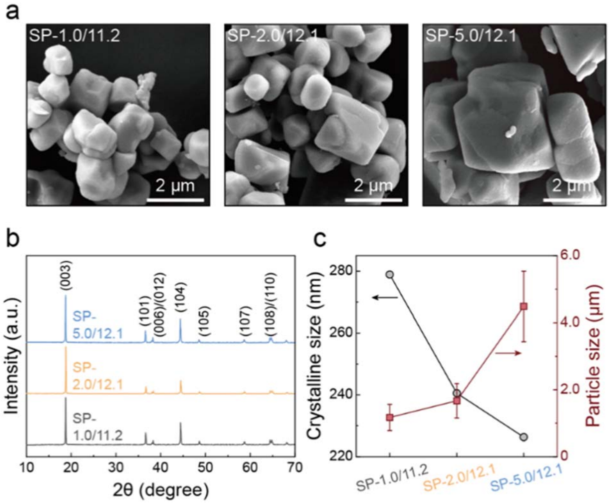

Fig. 3 (a) SEM images of Ni-rich single particle cathodes (SP-NCMs), SP-1.0/11.2, SP-2.0/12.1, and SP-5.0/12.1. The inset images depict the morphologies of the Ni-rich precursors prior to the molten-salt synthesis. The scale bar and the inset scale bar represent 2 μm and 500 nm, respectively. (b) XRD patterns of the three SP-NMC samples. (c) Overall crystalline and particle sizes of SP-1.0/11.2, SP-2.0/12.1, and SP-5.0/12.1. The error bars indicate the standard deviation of the measured particle sizes.

Open Access Article. Published on 13 March 2026. Downloaded on 6/14/2026 12:25:04 PM.
This article is licensed under a Creative Commons Attribution-NonCommercial 3.0 Unported Licence.

prominent crystalline faceting. The surfaces of SP-2.0/12.1 are enclosed by (001), (012), and (104) facets, as predicted by experimental observation and density-functional theory (DFT) calculations (Fig. S2).[39,40] The dominantly exposed crystal facets play a crucial role in determining the electrochemical stability, oxygen release, thermal decomposition, crystallographic reconstructions from layered to spinel or rock-salt, metal segregation, *etc.*[41,42] Among them, the (104) family facet is known to be most stable during electrochemical operations, whereas the (012) surface tends to be more reactive than the (001) surface, contributing to a higher initial discharge capacity but lower cycling stability.[43] In the case of SP-2.0/12.1, the predominant exposure of the (012) and (001) facets likely governs its distinctive electrochemical characteristics.

Fig. 3b presents the XRD patterns of SP-1.0/11.2, SP-2.0/12.1, and SP-5.0/12.1. All samples revealed an identical hexagonal α-$NaFeO_2$ type structure with the $R\bar{3}m$ space group without any other notable impurity phases, confirming the successful formation of the layered structure and the reliability of the synthesis process. Additionally, Rietveld refinement was performed to quantify the lattice parameters and the degree of Li/Ni cation mixing for the three samples (Fig. S3). The refined lattice parameters (a, c, and V) are nearly identical across the samples, whereas the Li/Ni cation mixing is ∼4% with a small but measurable variation of approximately ±0.5%. The overall domain sizes of the SP-NCM cathodes were estimated from the (003) peaks using the Scherrer equations, yielding coherent-crystalline sizes of 278.9, 240.5, and 226.3 nm for SP-1.0/11.2, SP-2.0/12.1, and SP-5.0/12.1, respectively (Fig. 3c). Interestingly, an inverse correlation between particle and Scherrer-based coherent domain size (003) sizes was observed; SP-1.0/11.2 exhibits the largest domain size despite having the smallest particle size. This phenomenon can be attributed to the relatively higher degree of recrystallization, promoted by the more porous precursor structure at the aggregate level. Conversely, the densely aggregated precursor, composed of thicker primary particles, produced the largest SP-NCM particle (SP-5.0/12.1) but exhibited the smallest domain size due to restricted recrystallization during the high-temperature molten-salt process. The inverse relationship between particle and domain sizes is a unique feature of the single-particle NCMs synthesized *via* our molten-salt route. To directly verify the internal domain structure corresponding to the XRD-based grain/domain-size trend, cross-sectional EBSD analysis was additionally conducted, confirming that SP-1.0/11.2 has a larger internal domain size while SP-2.0/12.1 and SP-5.0/12.1 show similarly smaller domains (Fig. S4 and S5). Furthermore, the intensity ratio between the (003) and (104) reflections, $I_{(003)}/I_{(104)}$, was identified as a structural quality indicator, given its sensitivity to cation mixing between Li^+ and M cations.[44,45] The measured $I_{(003)}/I_{(104)}$ ratios were 2.03, 3.43, and 2.18 in SP-1.0/11.2, SP-2.0/12.1, and SP-5.0/12.1, respectively. In general, the $I_{(003)}/I_{(104)}$ value exceeding 2.0 indicate a well-ordered layered structure, confirming that all SP-NCM samples possess high crystallinity with minimal cation disorder. Notably, SP-2.0/12.1 exhibited the highest $I_{(003)}/I_{(104)}$ ratio, suggesting the lowest degree of cation mixing. It should be noted, however, that structural morphology can also significantly affect the $I_{(003)}/I_{(104)}$. The well-grown truncated octahedron with dominant (001) facets in SP-2.0/12.1 likely contributes to its enhanced (003) peak intensity and correspondingly higher $I_{(003)}/I_{(104)}$.

The electrochemical responses of the SP-NCM cathodes are investigated, as shown in Fig. 4. The smaller particles (SP-1.0/11.2 and SP-2.0/12.1) exhibited higher utilization of Li^+ during the initial cycle at a rate of 0.1C (assuming $1C = 200$ mA g^{-1}). As shown in Fig. 4a, the initial discharge capacities of SP-1.0/11.2 and SP-2.0/12.1 were nearly the same, ∼192 mA h g^{-1}, whereas SP-5.0/12.1 delivered a slightly lower initial discharge capacity of ∼184 mA h g^{-1}. The initial cycle coulombic efficiencies (CEs) were 83.9%, 86.0%, and 82.7% for SP-1.0/11.2, SP-2.0/12.1, and SP-5.0/12.1, respectively. The highest quality of the layered structure in SP-2.0/12.1, as evidenced by the highest $I_{(003)/(104)}$ ratio, accounts for its highest CE. The cycling retention at a rate of 1C after two formation cycles showed that SP-1.0/11.2 and SP-2.0/12.1 maintained higher discharge capacities (∼179 mA h g^{-1}) than SP-5.0/12.1 (∼165 mA h g^{-1}), as shown in Fig. 4b. Again, SP-2.0/12.1 exhibited the highest CE among the samples even at the 1C rate, with initial CEs of 96.3%, 99.7%, and 96.3% for SP-1.0/11.2, SP-2.0/12.1, and SP-5.0/12.1, respectively. SP-2.0/12.1 also showed the highest capacity retention of ∼83.5% after 200 cycles, which is far more stable compared with commercial aggregate-level cathode structures. Its impressive cycling durability and rate performance are attributed to the high mechanical integrity of the single-particle structure, which effectively suppresses intergranular cracking. The remaining capacity fading is mainly caused by surface parasitic reaction and irreversible phase transformation during Li^+ (de)intercalation, as reported in the literature.

As shown in Fig. 4d–f, the structural stability of the SP-NCMs during cycling was evaluated by analyzing the differential capacity curves (dQ/dV *vs.* V). The corresponding cyclic voltammetry (CV) profiles at different scan rates are provided in Fig. S6. All samples showed four characteristic redox peaks,

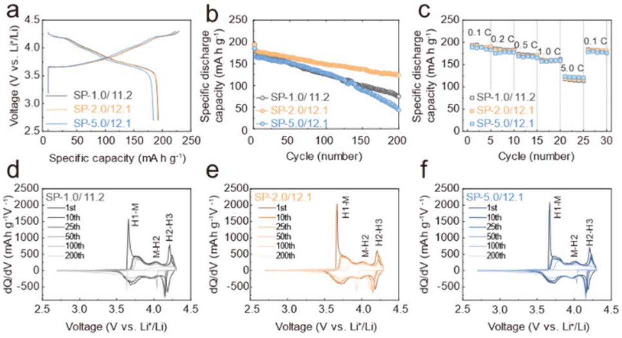

Fig. 4 Electrochemical performances of the SP-NCMs, SP-1.0/11.2, SP-2.0/12.1, and SP-5.0/12.1 at 25 °C. (a) Voltage profiles during the first cycle at a rate of 200 mA g^{-1}. (b) Cyclic performance at a rate of 200 mA g^{-1} for up to 200 cycles. The initial two formation cycles proceeded with a rate of 0.1C (20 mA g^{-1}). (c) Rate performances measured at different current densities. (d–f) dQ/dV *vs.* V plots in the range of 4.3–2.7 V (*vs.* Li/Li^+) for SP-1.0/11.2, SP-2.0/12.1, and SP-5.0/12.1, respectively.

Open Access Article. Published on 13 March 2026. Downloaded on 6/14/2026 12:25:04 PM.
This article is licensed under a Creative Commons Attribution-NonCommercial 3.0 Unported Licence.

corresponding to one second-order transition within the rhombohedral phase (H1) and three first-order transitions: H1 to monoclinic phase (M), M to hexagonal phase (H2), and H2 to the hexagonal phase (H3). For Ni-rich layered oxides (Ni > 0.9), the H2–H3 phase transition is often irreversible, owing to anisotropic lattice changes that induce mechanical strain within the particles, ultimately leading to a deterioration in cycling performances.[46] Therefore, the loss of the peak corresponding to the H2 to H3 transition is directly related to the irreversible loss of capacity.[47] As seen in Fig. 4d and f, the anodic peaks corresponding to the H2–H3 transition nearly disappear after 100 cycles for SP-1.0/11.2 and SP-5.0/12.1, indicating severe structural degradation. On the other hand, the H2–H3 phase transition is well preserved in SP-2.0/12.1, indicating the reversible Li (de)intercalation upon repeated cycling, which is related to the excellent cycle retention of SP-2.0/12.1.

Interestingly, contrary to the general expectation that a faster electrochemical response can be achieved in the smaller particles due to the larger reactive surface area to volume ratio and the shorter Li-ion diffusion path,[48] smallest and largest SP-NCM particles showed the best rate performance at the low and high current density, respectively as shown in Fig. 4c. This discrepancy suggests that the rate-limiting mechanism for Li^+ transport within SP-NCMs may vary with the applied current density. At lower cycling rates, the surface reaction kinetics likely dominate Li^+ (de)intercalation behavior, as evidenced by the smaller particles. This hypothesis is supported by the fact that the smallest particles with a larger surface-to-volume ratio exhibited the highest capacity retention at those lower rates. Conversely, at higher current densities, bulk diffusion becomes the primary rate-determining process. In this regime, the smaller domain size within the largest particles (SP-5.0/12.1) provides shorter diffusion pathways and enhanced Li^+ ionic conductivity within the bulk, resulting in a faster electrochemical response.

To further examine the kinetic contributions, the scan-rate dependence of peak current was analyzed using $i_p = av^b$. The fitted b-value is close to 1 in the low scan-rate region but gradually approaches 1/2 at higher scan rates, indicating a transition from a surface-controlled (capacitive-like) regime to a diffusion-controlled (solid-state diffusion limited) regime. Notably, SP-2.0/12.1 maintains the $b \approx 1$ behavior up to a relatively higher scan-rate (current) region, consistent with its reduced characteristic diffusion length due to the smaller particle size and internal domain size. The transition point shifts depending on the characteristic diffusion length scale, consistent with the combined influence of particle size and internal domain size (SI, Fig. S7).

To further examine the electrochemical kinetics of Li^+ transport during cycling, the lithium-ion diffusion coefficients (D_{Li^+}) were derived using the galvanostatic intermittent titration technique (GITT), as originally proposed by Weppner and Huggins.[49] The GITT measurements were carried out with a voltage range of 2.7–4.3 V over five cycles. The corresponding time–voltage profiles obtained during GITT experiments are presented in Fig. 5a and b. The lithium-ion diffusion coefficient was calculated using the following equation.[50]

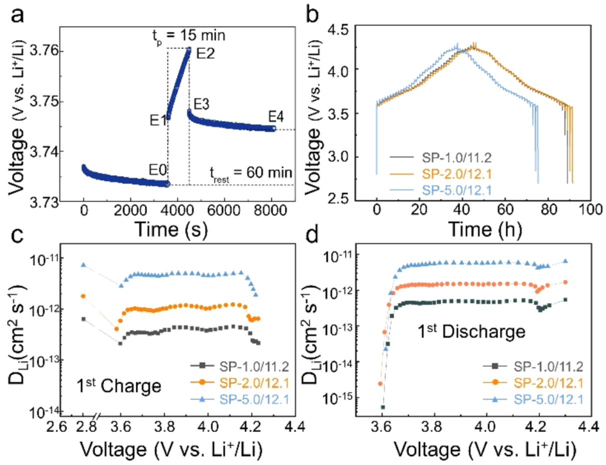

Fig. 5 (a) Zoomed voltage *vs.* time profile for a representative GITT titration step at 3.7371 V. (b) GITT curves of SP-NCMs during the first cycle. Lithium-ion diffusion coefficients calculated for the first (c) charge and (d) discharge process.

$$D_{Li^+} = \frac{4}{9\pi} \cdot \left(\frac{E_4 - E_0}{E_3 - E_0}\right) \cdot \frac{{r_P}^2}{t_P}. \tag{1}$$

The parameters, D_{Li^+} ($cm^2\ s^{-1}$), t_p (s), and r_p (cm), represent the lithium-ion diffusion coefficient, pulse time, and radius of particles, respectively, as illustrated in Fig. 5a. Upon initiation of the charging process, D_{Li^+} value decreased by approximately fourfold during the second-order H1 phase transition. Subsequently, the diffusion coefficient partially recovered and remained relatively stable throughout the continued charging process. A further ∼50% drop in D_{Li^+} was observed near ∼4.1 V, corresponding to the H2–H3 transition, where significant volume changes occur (Fig. 5c). The variation in D_{Li^+} during discharge has a symmetrical trend to that observed during charge, suggesting Li^+ intercalation and deintercalation follow the same reaction pathway. The highest average D_{Li^+} value ($5.80 \times 10^{-12}\ cm^2\ s^{-1}$) was observed for the largest SP particle, SP-5.0/12.1. The enhanced Li^+ diffusion coefficient in the largest SP-NCM particles can be ascribed to their smallest domain size, which facilitates shorter diffusion paths within the bulk. Because the GITT expression explicitly depends on the characteristic length scale (${r_p}^2$), we additionally compared a normalized metric, $D/{r_p}^2$, to mitigate geometric effects associated with particle size (SI, Fig. S8). The normalized values show only small differences across samples, suggesting broadly similar intrinsic diffusivity. Notably, SP-2.0/12.1 exhibits a slightly higher $D/{r_p}^2$, indicating marginally more favorable effective transport kinetics. Importantly, despite its larger particle size, SP-5.0/12.1 shows a comparable $D/{r_p}^2$ relative to the other samples, suggesting that the internal domain size can strongly influence the effective diffusion length and compensate for particle-size effects. Overall, these results indicate that the effective Li^+ transport is influenced by the combined contribution of particle size and internal domain size (*i.e.*, the effective diffusion length) rather than particle size alone. Synthetically, the normalized $D/{r_p}^2$ analysis and the domain-size characterization suggest that

Open Access Article. Published on 13 March 2026. Downloaded on 6/14/2026 12:25:04 PM.
This article is licensed under a Creative Commons Attribution-NonCommercial 3.0 Unported Licence.

the effective Li^+ transport is governed by the characteristic diffusion length determined by both particle size and internal domain size. Notably, SP-5.0/12.1 shows a comparable D/r_p^2 despite its larger particle size, supporting that internal domain size can compensate for particle-size effects by shortening the effective diffusion length. Moreover, the lithium-ion diffusion coefficients remained stable up to the fifth cycle (Fig. S9), demonstrating the kinetic robustness of the SP-NCM cathodes during prolonged operation.

The physical and chemical stability of SP-NCM cathode particles was studied by postmortem analysis. In conventional polycrystal NCMs with aggregated secondary structure, repeated anisotropic change along the *c*- and *a*-axis typically results in the formation of intergranular cracks during prolonged cycles.[51–53] However, SP-NCM cathode particles show neither visible inter- nor intragranular fractures even after 200 cycles, as evidenced by cross-sectional SEM (Fig. 6a). As shown in Fig. 6b, the chemical stability of the SP-NCM cathode was further evaluated by Ni 2p X-ray photoelectron spectroscopy (XPS).[54–57] The quantitative analysis reveals that the Ni^{3+} fraction follows the order of SP-2.0/12.1 > SP-1.0/11.2 > SP-5.0/12.1, which is perfectly aligned with the long-term cycling stability results presented in Fig. 4b.

This stability trend is governed by the synergistic effect of particle size and crystalline domain size. SP-2.0/12.1 represents an optimized balance that minimizes the specific surface area while maintaining high crystalline integrity, resulting in the highest Ni^{3+} ratio and superior chemical stability. In contrast, SP-5.0/12.1, despite having the largest particle size, possesses the smallest crystalline domain size, leading to a high density of internal grain boundaries that intersect the particle surface. These boundaries act as active sites for surface reduction (Ni^{2+} formation) and localized phase transitions. Crucially, even without macroscopic mechanical fractures, this domain boundary-mediated chemical degradation ultimately accelerates capacity fading. Conversely, SP-1.0/11.2 maintains a large domain size but suffers from an excessively high specific surface area, which promotes greater electrolyte contact and unavoidable surface reduction.[58,59] These findings collectively clarify that the superior performance of SP-2.0/12.1 is due to the successful decoupling and control of particle and domain size effects, ensuring enhanced structural and electrochemical robustness.

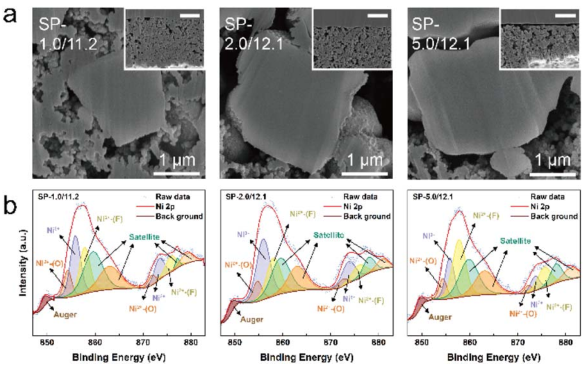

Fig. 6 (a) Cross-sectional SEM images of SP-1.0/11.2, SP-2.0/12.1, and SP-5.0/12.1 particles after 200 cycles at a rate of 1C. Low magnification images are shown in the insets. The main and inset scale bars indicate 1 μm and 10 μm, respectively. (b) Ni 2p XPS spectra of SP-1.0/11.2, SP-2.0/12.1, and SP-5.0/12.1 after 200 cycles at a rate of 1C.

4. Conclusion

In summary, single-particle NCM cathodes were successfully synthesized through a two-step scalable process combining controlled coprecipitation and a subsequent molten-salt reaction. By precisely tuning the precursor morphology through ammonia concentration and pH, we enabled systematic control over both the final particle size and crystalline domain size in the synthesized cathode materials. This study demonstrates that the crystalline domain size governs the rate performance, while the specific surface area and the density of internal domain boundaries, determined by the particle size and domain size, primarily dictate the chemical and electrochemical stability. These insights establish a fundamental understanding of how to optimize rate capability and structural durability in single-particle Ni-rich NCM cathodes, offering a practical route to mitigate surface-driven degradation while retaining high performance. The findings presented here are expected to guide the design of next-generation layered oxide cathode materials with enhanced kinetic and structural stability for advanced lithium-ion batteries.

Author contributions

Soonhyun Hong: writing – original draft, visualization, validation, software, methodology, investigation, formal analysis, data curation, conceptualization. Heesang Lee: writing – original draft, visualization, software, methodology, investigation, formal analysis, data curation. Jahun Koo: visualization, software, methodology, investigation, formal analysis, data curation. Wonchan Hwang: visualization, software, methodology, investigation, formal analysis, data curation. Ji Hwan Kim: visualization, software, methodology, investigation, formal analysis, data curation. Jungjin Park: writing – review & editing, validation, supervision, project administration, funding acquisition, conceptualization. Young-Sang Yu: writing – review & editing, validation, supervision, project administration, funding acquisition, conceptualization. Chunjoong Kim: writing – review & editing, validation, supervision, project administration, funding acquisition, conceptualization.

Conflicts of interest

There are no conflicts of interest to declare.

Data availability

The data supporting this article have been included as part of the supplementary information (SI). Supplementary information: detailed experimental procedures, additional SEM images with EBSD domain maps, XRD with Rietveld refinement and electrochemical impedance spectroscopy (EIS) data. See DOI: https://doi.org/10.1039/d5ta10228f.

This journal is © The Royal Society of Chemistry 2026

Open Access Article. Published on 13 March 2026. Downloaded on 6/14/2026 12:25:04 PM. This article is licensed under a Creative Commons Attribution-NonCommercial 3.0 Unported Licence.

Acknowledgements

S. H. and H. L. contributed equally to this work. C. K. was supported through the National Research Foundation of Korea (NRF) funded by the Ministry of Science and ICT (RS-2023-NR077186) and the Ministry of Education (RS-2021-NR060128). Y.-S. Y. was supported by the Commercialization Promotion Agency for R&D Outcomes (COMPA) grant funded by the Korean Government (Ministry of Science and ICT, Grant No. RS-2023-00304768). This work was supported by the KIST Institutional Program (No. 26E0321 and No. 26E0324).

References

1 S. Fankhauser, S. M. Smith, M. Allen, K. Axelsson, T. Hale, C. Hepburn, J. M. Kendall, R. Khosla, J. Lezaun, E. Mitchell-Larson, M. Obersteiner, L. Rajamani, R. Rickaby, N. Seddon and T. Wetzer, *Nat. Clim. Change*, 2022, **12**, 15–21.

2 H. E. Melin, *The lithium-ion battery end-of-life market – A baseline study*, World Economic Forum, 2018.

3 N. Nitta, F. X. Wu, J. T. Lee and G. Yushin, *Mater. Today*, 2015, **18**, 252–264.

4 K. Mizushima, P. C. Jones, P. J. Wiseman and J. Goodenough, *Solid State Ionics*, 1981, **3–4**, 171–174.

5 S. Watanabe, M. Kinoshita, T. Hosokawa, K. Morigaki and K. Nakura, *J. Power Sources*, 2014, **260**, 50–56.

6 X. Wu, K. Song, X. Zhang, N. Hu, L. Li, W. Li, L. Zhang and H. Zhang, *Front. Energy Res.*, 2019, **7**, 65.

7 L. K. Willenberg, P. Dechent, G. Fuchs, D. U. Sauer and E. Figgemeier, *Sustainability*, 2020, **12**, 557.

8 J. Li, A. R. Cameron, H. Y. Li, S. Glazier, D. J. Xiong, M. Chatzidakis, J. Allen, G. A. Botton and J. R. Dahn, *J. Electrochem. Soc.*, 2017, **164**, A1534–A1544.

9 H.-H. Ryu, B. Namkoong, J.-H. Kim, I. Belharouak, C. S. Yoon and Y.-K. Sun, *ACS Energy Lett.*, 2021, **6**, 2726–2734.

10 L. De Biasi, A. Schiele, M. Roca-Ayats, G. Garcia, T. Brezesinski, P. Hartmann and J. Janek, *ChemSusChem*, 2019, **12**, 2240–2250.

11 J. Zhang, J. Zhang, X. Ou, C. Wang, C. Peng and B. Zhang, *ACS Appl. Mater. Interfaces*, 2019, **11**, 15507–15516.

12 K.-J. Park, J.-Y. Hwang, H.-H. Ryu, F. Maglia, S.-J. Kim, P. Lamp, C. S. Yoon and Y.-K. Sun, *ACS Energy Lett.*, 2019, **4**, 1394–1400.

13 H. Li, A. Liu, N. Zhang, Y. Wang, S. Yin, H. Wu and J. R. Dahn, *Chem. Mater.*, 2019, **31**, 7574–7583.

14 P. Xiao, T. Shi, W. Huang and G. Ceder, *ACS Energy Lett.*, 2019, **4**, 811.

15 G.-T. Park, H.-H. Ryu, T.-C. Noh, G.-C. Kang and Y.-K. Sun, *Mater. Today*, 2022, **52**, 9–18.

16 Y. Liu, X. Fan, B. Luo, Z. Zhao, J. Shen, Z. Liu, Z. Xiao, B. Zhang, J. Zhang and L. Ming, *J. Colloid Interface Sci.*, 2021, **604**, 776–784.

17 K. Park, D. J. Ham, S. Y. Park, J. Jang, D.-H. Yeon, S. Moon and S. J. Ahn, *RSC Adv.*, 2020, **10**, 26756–26764.

18 L. Zheng, J. C. Bennett and M. N. Obrovac, *J. Electrochem. Soc.*, 2020, **167**, 130536.

19 J. E. Harlow, X. Ma, J. Li, E. Logan, Y. Liu, N. Zhang, L. Ma, S. L. Glazier, M. M. E. Cormier and M. Genovese, *J. Electrochem. Soc.*, 2019, **166**, A3031–A3044.

20 J. Cheng, X. Ma, X. Sun, F. Lian, X. Liu, L. Lu and D. Xia, *Energy Storage Mater.*, 2025, **79**, 104332.

21 Y. Han, S. H. Jung, H. Kwak, S. Jun, H. H. Kwak, J. H. Lee, S. T. Hong and Y. S. Jung, *Adv. Energy Mater.*, 2021, **11**, 2100126.

22 A. Chen, K. Wang, J. Li, Q. Mao, Z. Xiao, D. Zhu, G. Wang, P. Liao and J. He, *Front. Energy Res.*, 2020, **8**, 593009.

23 J. Li, H. Li, W. Stone, R. Weber, S. Hy and J. R. Dahn, *J. Electrochem. Soc.*, 2017, **164**, A3529.

24 H. Li, J. Li, N. Zaker, N. Zhang, G. A. Botton and J. R. Dahn, *J. Electrochem. Soc.*, 2019, **166**, A1956.

25 M. H. Lee, Y. J. Kang, S. T. Myung and Y. K. Sun, *Electrochim. Acta*, 2004, **50**, 939–948.

26 L. Liang, K. Du, Z. Peng, Y. Cao, J. Duan, J. Jiang and G. Hu, *Electrochim. Acta*, 2014, **130**, 82–89.

27 C. Deng, L. Liu, W. Zhou, K. Sun and D. Sun, *Electrochim. Acta*, 2008, **53**, 2441–2447.

28 F. Lv, Y. Zhang, M. Wu and Y. Gu, *Small*, 2022, **18**, 2201946.

29 C. A. Schneider, W. S. Rasband and K. W. Eliceiri, *Nat. Methods*, 2012, **9**, 671–675.

30 F. Peng, D. Mu, R. Li, Y. Liu, Y. Ji, C. Dai and F. Ding, *RSC Adv.*, 2019, **9**, 21922–21930.

31 K.-M. Nam, H.-J. Kim, D.-H. Kang, Y.-S. Kim and S.-W. Song, *Green Chem.*, 2015, **17**, 1127–1135.

32 Y. Yang, S. Xu, M. Xie, Y. He, G. Huang and Y. Yang, *J. Alloys Compd.*, 2015, **619**, 846–853.

33 P. L. Guzzo, A. A. A. Tino and J. B. Santos, *Powder Technol.*, 2015, **284**, 122–129.

34 J. Huang, P. Xu, D. Cao, X. Zhou, S. Yang, Y. Li and G. Wang, *J. Power Sources*, 2014, **246**, 371–376.

35 R. Wang, J. Lang, Y. Liu, Z. Lin and X. Yan, *NPG Asia Mater.*, 2015, **7**, e183.

36 L. Qiu, M. Zhang, Y. Ming, Y. Song, C. Xu, Z. Wu, Q. Xu, T. Chen, G. Wang and Y. Liu, *Chem. Eng. Sci.*, 2021, **233**, 116337.

37 Z. Wu, Y. Zhou, C. Hai, J. Zeng, X. Ren, Y. Sun, Y. Shen, X. Li, S. Dong and G. Zhang, *Ceram. Int.*, 2022, **48**, 17279–17288.

38 J. Langdon and A. Manthiram, *Energy Storage Mater.*, 2021, **37**, 143–160.

39 T. Wang, K. Ren, M. He, W. Dong, W. Xiao, H. Pan, J. Yang, Y. Yang, P. Liu and Z. Cao, *Front. Chem.*, 2020, **8**, 747.

40 J. C. Garcia, J. Bareño, J. Yan, G. Chen, A. Hauser, J. R. Croy and H. Iddir, *J. Phys. Chem. C*, 2017, **121**, 8290–8299.

41 S. Sharifi-Asl, F. A. Soto, A. Nie, Y. Yuan, H. Asayesh-Ardakani, T. Foroozan, V. Yurkiv, B. Song, F. Mashayek and R. F. Klie, *Nano Lett.*, 2017, **17**, 2165–2171.

42 P. Yan, J. Zheng, J. Zheng, Z. Wang, G. Teng, S. Kuppan, J. Xiao, G. Chen, F. Pan and J.-G. Zhang, *Adv. Energy Mater.*, 2016, **6**, 1502455.

43 J. Zhu and G. Chen, *J. Mater. Chem. A*, 2019, **7**, 5463–5474.

44 H. J. Kim, Y. Park, Y. Kwon, J. Shin, Y.-H. Kim, H.-S. Ahn, R. Yazami and J. W. Choi, *Energy Environ. Sci.*, 2020, **13**, 286–296.

Open Access Article. Published on 13 March 2026. Downloaded on 6/14/2026 12:25:04 PM.
This article is licensed under a Creative Commons Attribution-NonCommercial 3.0 Unported Licence.

45 S. Sloop, L. Crandon, M. Allen, K. Koetje, L. Reed, L. Gaines and W. Sirisaksoontorn, *Sustain. Mater. Technol.*, 2020, **25**, e00152.

46 J. Lai, J. Zhang, Z. Li, Y. Xiao, W. Hua, Z. Wu, Y. Chen, Y. Zhong and W. Xiang, *Chem. Commun.*, 2020, **56**, 4886–4889.

47 J. Xu, E. Hu, D. Nordlund, A. Mehta, S. N. Ehrlich, X. Q. Yang and W. Tong, *ACS Appl. Mater. Interfaces*, 2016, **8**, 31677–31683.

48 B. Kang and G. Ceder, *Nature*, 2009, **458**, 190–193.

49 W. Weppner and R. A. Huggins, *J. Electrochem. Soc.*, 1977, **124**, 1569.

50 A. Nickol, T. Schied, C. Heubner, M. Schneider, A. Michaelis, M. Bobeth and G. Cuniberti, *J. Electrochem. Soc.*, 2020, **167**, 090546.

51 F. Zhang, S. Lou, S. Li, Z. Yu, Q. Liu, A. Dai, C. Cao, M. F. Toney, M. Ge and X. Xiao, *Nat. Commun.*, 2020, **11**, 3050.

52 J. Li and A. Manthiram, *Adv. Energy Mater.*, 2019, **9**, 1902731.

53 J. Li, L. E. Downie, L. Ma, W. Qiu and J. R. Dahn, *J. Electrochem. Soc.*, 2015, **162**, A1401.

54 Y. Wang, S. Tao, H. Lin, S. Han, W. Zhong, Y. Xie, J. Hu and S. Yang, *RSC Adv.*, 2020, **10**, 33475–33482.

55 Y. S. Chen, J. F. Kang, B. Chen, B. Gao, L. F. Liu, X. Y. Liu, Y. Y. Wang, L. Wu and H. Y. Yu, *J. Phys. D: Appl. Phys.*, 2012, **45**, 065303.

56 N. S. Mcintyre, T. C. Chan and C. Chen, *Oxid. Met.*, 1990, **33**, 457–479.

57 R. Hang, X. Huang, L. Tian, Z. He and B. Tang, *Electrochim. Acta*, 2012, **70**, 382–393.

58 J. Kim, H. Cha, H. Lee, P. Oh and J. Cho, *Batter. Supercaps*, 2020, **3**, 309–322.

59 Y. Kim, *ACS Appl. Mater. Interfaces*, 2012, **4**, 2329.

This journal is © The Royal Society of Chemistry 2026